



## On the reactive sintering of Heusler Fe<sub>2</sub>VAl-based thermoelectric compounds

Camille van der Rest<sup>a</sup>, Védi Dupont<sup>b</sup>, Jean-Pierre Erauw<sup>b</sup>, Pascal J. Jacques<sup>a,\*</sup>

<sup>a</sup> UCLouvain, Institute of Mechanics, Materials and Civil Engineering, IMAP, Place Sainte Barbe 2, B-1348, Louvain La Neuve, Belgium

<sup>b</sup> Belgian Ceramic Research Centre (BCRC), Avenue Gouverneur Cornez 4, B-7000, Mons, Belgium

### ARTICLE INFO

#### Keywords:

Fe<sub>2</sub>VAl  
Heusler compounds  
Thermoelectric materials  
Field-assisted/spark plasma reactive sintering  
Reaction path  
Microstructure

### ABSTRACT

Heusler Fe<sub>2</sub>VAl-based compounds are promising candidates for thermoelectric conversion of waste heat. In comparison to more conventional thermoelectric materials, the constitutive elements of these alloys are indeed abundant, cheap, and non-toxic. Furthermore, the thermoelectric properties of these compounds can be easily enhanced by either doping or controlled deviation from exact stoichiometry while large power factors compatible with energy harvesting applications can be reached.

In the present study, Fe<sub>2</sub>VAl-based compounds were synthesised by powder metallurgy. Almost fully dense bulk materials were obtained either by field-assisted sintering, also referred to as spark plasma sintering (SPS), of pre-alloyed powders or by spark plasma reactive sintering of mixtures of elemental powders. The influence of the processing route and parameters on the resulting microstructure was assessed. In the specific case of the one-step synthesis and rapid densification of the Fe<sub>2</sub>VAl compound starting from the elemental powders, a detailed insight in the reaction path was obtained by interrupted sintering cycles followed by careful phase analysis of the partially sintered compacts by X-ray diffraction and elemental analysis. Finally, it is worth emphasising that the thermoelectric properties of the compounds processed by reactive sintering are as good as the ones of samples sintered from pre-alloyed powder or processed by melting and casting.

### 1. Introduction

Fe-based Heusler compounds perfectly fit the requirements of large-scale waste heat harvesting applications, owing to the availability and low cost of their constitutive elements, in addition to their good thermoelectric properties. However, these intermetallic compounds remain brittle and require specific processing routes. Powder metallurgy is commonly used to manufacture bulk thermoelectric materials with the main advantage of being a solid-state process, thus limiting the issues of embrittlement during solidification or contamination in the case of reactive liquid [1]. Cook and Haringa emphasised the interest of solid-state synthesis, contrarily to more traditional melt-grow processes, to obtain novel compositions and refined microstructures [2]. In addition, powder metallurgy allows processing near-net-shape samples which can be used without additional steps in thermoelectric modules.

Powder metallurgy starts from powder(s) that, after being shaped into a compact, are densified by sintering, i.e. by applying a heat treatment below the melting temperature, with or without concurrently applying an external mechanical pressure [3]. Furthermore,

field-assisted sintering, also referred to as spark plasma sintering (SPS), allows faster consolidation, thus bringing advantages like reduced grain growth. As mentioned by Belov et al. [4] for Bi<sub>2</sub>Te<sub>3</sub>, but also for other compounds like Fe<sub>2</sub>VAl, sintering can be applied to powders of previously synthesised material (with directly the stoichiometric composition), to mixtures of elemental powders in stoichiometric ratio or to mixtures between binary or ternary alloys supplemented with elemental powder(s) in order to achieve the right composition. While some authors studied the synthesis of iron aluminides from elemental powders [5–10], the original aspect of this research is the consideration of reactive sintering for Fe<sub>2</sub>VAl-based thermoelectric compounds. Thereupon, this reactive sintering approach is performed in the current study using one of the field-assisted sintering processes, namely spark plasma sintering (SPS), that have emerged in recent years, allowing faster densification of the powder compacts and bringing accordingly advantages like reduced grain growth or lower sintering temperatures.

The present work has been divided into three experimental parts: the analysis of the reaction path of mixed elemental Fe, V, and Al powders, the characterisation of the densification behaviour of a pre-alloyed

\* Corresponding author.

E-mail address: [pascal.jacques@uclouvain.be](mailto:pascal.jacques@uclouvain.be) (P.J. Jacques).

Fe<sub>2</sub>VAl powder by spark plasma sintering, and the analysis of the reactive sintering behaviour of mixed elemental powders. Finally, a comparison between sintered samples from pre-alloyed and from mixed elemental powders was carried out.

## 2. Materials and experimental procedure

For the assessment of the reaction path and reactive sintering experiments, high purity elemental powders were provided by Alfa Aesar: iron (98.0 % purity), aluminium (99.5 % purity) and vanadium (99.8 % purity) with  $d_{50}$  values of 22  $\mu\text{m}$ , 19  $\mu\text{m}$  and 23  $\mu\text{m}$ , respectively. These powders were weighted in stoichiometric proportions and mixed in a SpeedMixer device, working by dual asymmetric centrifugation and thus providing fast high-energy mixing. The pre-alloyed Fe<sub>2</sub>VAl powder (provided by Goodfellow Ltd.) used as reference material had a larger median particle size ( $d_{50}$ , around 76  $\mu\text{m}$ ). It was synthesised by atomisation of the molten alloy followed by a crushing step.

The different heat treatments were carried out on a HP D 25/1 SPS equipment (FCT Systeme GmbH, Germany) under vacuum. For the assessment of the reaction path, the mixed elemental powders were pre-compacted externally under a load of 195 MPa before pressureless sintering experiments conducted in the SPS equipment using an adapted graphite tool in the temperature range 873–1473 K. For the determination of the densification behaviour, the powders were pre-compacted directly in the 20 mm diameter graphite die of the SPS equipment. In the case of the pre-alloyed powder, the selected load (in the range of 20–60 MPa) was applied from the start and kept constant throughout the thermal cycle. For the reactive sintering runs starting from the mixed elemental powders, a minimum load of 10 MPa was applied after pre-compaction (45 MPa) and maintained up to 1273 K before increasing it to the selected maximal value in order to avoid expelling the aluminium above its melting temperature. The axial displacements of the plungers were recorded continuously during the SPS runs, enabling the monitoring of the densification with time for the different conditions investigated. The temperature was measured using an axial pyrometer focussing through the hollow upper plunger on a surface located about 2 mm above the specimen. In the pressureless experiments, owing to the modified tool configuration and absence of direct contact between the powder compact and the upper punch, a difference between the recorded and real temperatures of the compact is anticipated. The imposed heating rate was 50 K min<sup>-1</sup>. The dwell duration was 15 min.

The apparent density and percentage of open porosity of the sintered samples were measured using Archimedes' water immersion method. Their relative density was calculated according to Equation (1) using a theoretical density value of 6.5837 g cm<sup>-3</sup>, corresponding to the true density of the pre-alloyed powder as measured by Helium pycnometry.

$$\rho_{rel} = \frac{\rho_{app}}{\rho_{theor}} \cdot 100 \quad (1)$$

The resulting microstructures of the (reactively) sintered samples were characterised by scanning electron microscopy (SEM - Carl Zeiss Ultra-55) and by electron backscatter diffraction (EBSD) with mounted and polished samples. In addition, energy-dispersive X-ray spectroscopy (EDX) was coupled to SEM for the local chemical characterisation of the samples. Elemental mapping was carried out in order to scrutinise the reaction path. The identification of the phases was carried out by X-ray diffraction analyses (XRD - Bruker AXS - D8 Advance diffractometer) using a Cu K<sub>α1</sub> source ( $\lambda = 1.5406 \text{ \AA}$ ). The thermal analysis of the mixed powders was performed with a Netzsch STA 409 instrument. The thermoelectric properties (Seebeck coefficient and electrical resistivity) were characterised simultaneously with a Netzsch SBA 458 Nemesis.

## 3. Experimental results

### 3.1. Reaction path of mixed elemental powders

Fig. 1 presents SEM micrographs (back-scattered electrons) of pre-compacted mixed elemental Fe, V, and Al powders heated to 873 K and 1473 K (pressureless sintering), respectively. This figure highlights a significant difference of the chemical homogeneity between these two samples. At 873 K, at least three phases are observed, while at 1473 K the sample seems more homogeneous.

Fig. 2 presents EDX elemental mapping analyses of mixed powders after interrupted heating cycle at different temperatures up to 1473 K. These maps clearly show the reaction of Al (highlighted in blue) with the edges of the Fe particles (in red) already at 873 K. Local EDX analyses corroborate this observation with a composition of the Al-rich phase of 34 at.% Fe – 1 at.% V – 65 at.% Al. Similar results are obtained when interrupting the heating cycle at 873 K or 973 K. In the temperature range from 1073 K to 1173 K, a phase richer in Fe forms (69 at.% Fe – 1 at.% V – 30 at.% Al) that coexists with the previous Al-rich phase. Further diffusion of Al occurs within the core of Fe particles: from 0.3 at.% Al at 873 K to 17 at.% Al at 1273 K, temperature at which no more Al-rich phase is present. When 1373 K is reached, no more “pure” Fe particles are visible. At this stage, Al is supposed to have homogeneously diffused within the Fe particles. Vanadium particles stay almost pure (>97 at.% V) up to 1473 K, when some ternary phases appear on their edges. Accordingly, the Fe-Al phases are enriched in V: < 1 at.% V below 1073 K, 1–2 at.% V up to 1373 K, and 8 at.% V at 1473 K. In addition to chemical reactions, Fig. 2(d)-(h) show that bonding occurs between the Fe/Al and V particles starting from 1073 K.

Fig. 3 presents the X-ray diffractograms corresponding to the elemental mapping analyses of Fig. 2. At 873 K, the Al peak is not present anymore. From 973 K to 1373 K, the Fe peak progressively disappears while Fe<sub>2</sub>Al<sub>5</sub> and FeAl peaks appear up to 1073 K and 1373 K, respectively. At 1473 K, the V peak shrinks and some intermediate phase between FeAl and Fe<sub>2</sub>VAl simultaneously appears.

Heating the mixed elemental powders at 50 K min<sup>-1</sup> up to 1473 K is not enough to obtain a Fe<sub>2</sub>VAl single phase (Fig. 2(h) and Fig. 3). Consequently, a dwell of 15 min was applied at high temperature to further promote diffusion. Fig. 4 presents EDX superimposed and individual mapping analyses of mixed powders after heating up to 1473 K and with an additional dwell of 15 min. As mentioned above (Fig. 2(h)), the reaction of Al and Fe with the V particles is very limited after heating to 1473 K. The individual maps of Fig. 4(b) show that diffusion progresses significantly during the 15 min-dwell, leading to almost a full single ternary composition. Fig. 5 presents the corresponding X-ray diffractograms with the vanadium peak that almost vanishes after this 15 min-dwell, while the FeAl peak clearly shifts towards the Fe<sub>2</sub>VAl peak due to enrichment in vanadium. A small V peak is still hardly visible on Fig. 5 after the 15 min dwell at 1373 K. While diffusion progresses during heating between 1373 K and 1473 K, almost no difference remains between the samples sintered at those temperatures after the 15 min dwell. A look at a larger 2 $\theta$ -range on Fig. 6 highlights the presence of the different peaks of the Fe<sub>2</sub>VAl ordered phase L<sub>21</sub>, e.g. (111) and (200), for the sample sintered at 1473 K.

### 3.2. Densification of pre-alloyed powder

Prior to the densification of mixed elemental powder compacts, the sintering behaviour of the pre-alloyed Fe<sub>2</sub>VAl powder was investigated and the SPS conditions leading to near-full density compacts were determined. It is worth noting that the presence of the (111) and (200) peaks typical of the ordered L<sub>21</sub> structure was confirmed by XRD, even for the samples sintered at the highest temperature. Fig. 7 shows the evolution of the relative density of sintered samples as a function of the dwell temperature and applied pressure, with an emphasis on the 98 % threshold. As it could be expected, the relative density of sintered

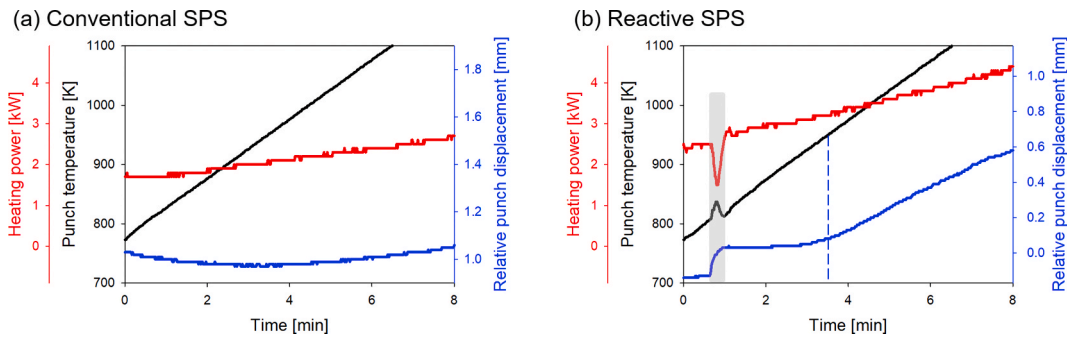


Fig. 1. SEM micrographs (back-scattered electrons) of mixed elemental powders after interrupted pressureless sintering heating cycle at (a) 873 K and (b) 1473 K.

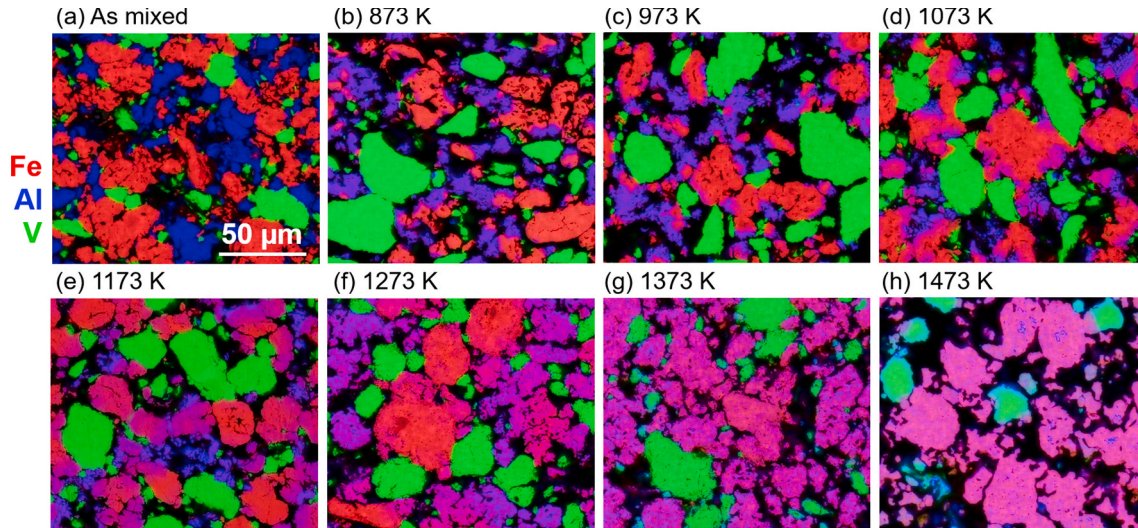


Fig. 2. Typical EDX maps illustrating the evolution of mixed elemental powders (a) when interrupting the heating cycle at various temperatures: (b) 873 K, (c) 973 K, (d) 1073 K, (e) 1173 K, (f) 1273 K, (g) 1373 K, and (h) 1473 K. Fe is highlighted in red, V in green, and Al in blue. Identical scale for the different maps.

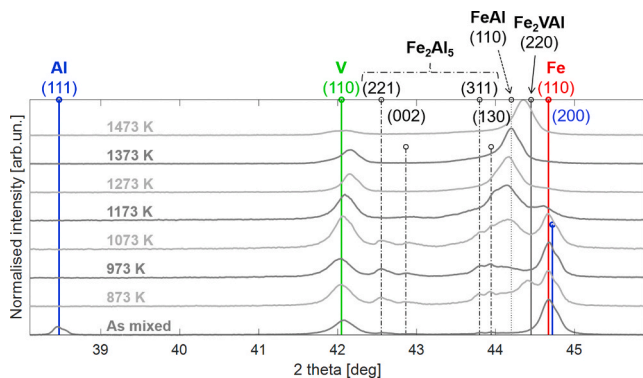


Fig. 3. X-ray diffractograms of mixed elemental powders when interrupting the heating cycle every 100 K during pressureless sintering. The theoretical peak positions of various phases are shown: Al in blue, V in green,  $\alpha$ -Fe in red,  $\text{Fe}_2\text{Al}_5$  in dashed-dotted black, FeAl in dotted black and  $\text{Fe}_2\text{VAI}$  in black.

samples increases with increasing applied pressure and temperature. However, at the highest temperature (1523 K), a slight decrease of the relative density is observed. This phenomenon may be due to the thermal dilatation of gases trapped in closed porosities, referred to in the literature as desintering [11,12], but also to the higher reactivity of the powder compact with the graphite tooling, giving rise to the formation of more carbides. SEM analyses, coupled with EDX, confirm that the proportion of vanadium carbides VC in the material increases from 0.25

% to 1.72 % when sintering at 1523 K instead of 1473 K. It leads in turn to slight changes of the final composition and hence to some inaccuracy in the considered theoretical density. The optimized conditions leading to relative density values larger than 98 %, are thus a dwell temperature in the 1423–1473 K range and an applied pressure larger than 40 MPa. The sample sintered 15 min at 1473 K under 40 MPa reached the highest relative density of 99.3 %.

### 3.3. Densification of mixed elemental powders

Based on the above results for the reaction path of mixed elemental powders and for the densification of the pre-alloyed powder, it is expected that a spark plasma reactive sintering cycle of 15 min at 1473 K under 40 MPa of a mixed elemental powders compact would lead to dense, homogeneous and fully reacted  $\text{Fe}_2\text{VAI}$  sintered samples.

Fig. 8 compares the apparent density values of both pressureless and pressure-assisted reactively sintered mixed elemental powders compacts. The apparent density is reported here since the theoretical density has not been assessed for each intermediate stage of the reaction path, thus preventing the calculation of a relative density as done previously (see Equation (1)). In the case of pressureless conditions, no significant evolution of the apparent density is observed over the whole investigated temperature range. The 15 min dwell has only a limited influence on the apparent density (slight increase by 5–7 %) and on the open porosity, that remains around 48–49 %, regardless of the dwell temperature. Based on the results presented in Section 3.1, especially the diffractogram of Fig. 6, it is assumed that the compact heat treated for 15 min at 1473 K is fully reacted and composed of the desired  $\text{L}_2\text{Fe}_2\text{VAI}$

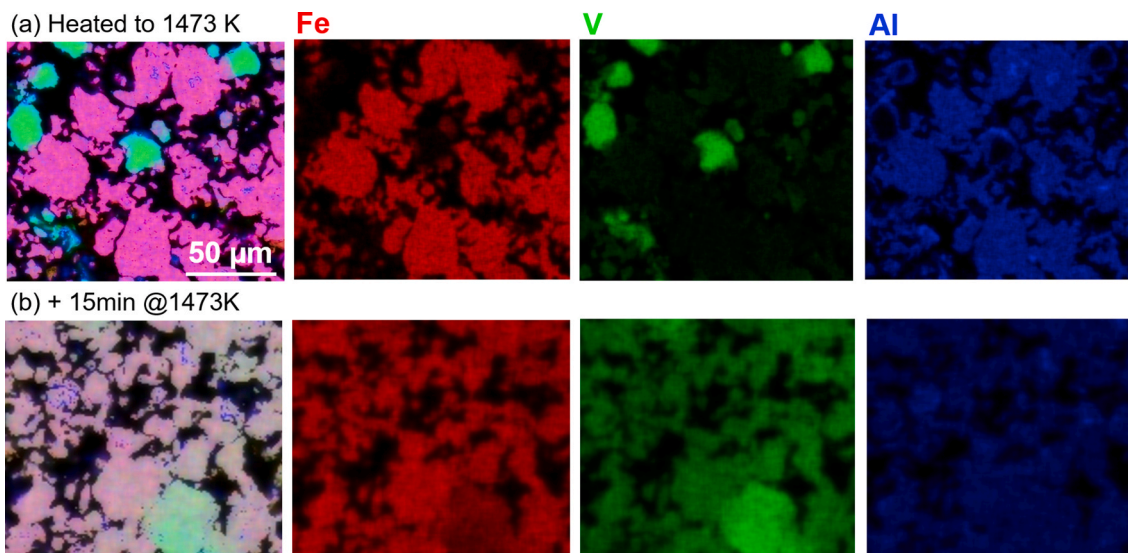


Fig. 4. Superimposed and individual EDX maps illustrating the evolution of mixed elemental powders (a) when heating to 1473 K and (b) with an additional dwell of 15 min. Fe is highlighted in red, V in green, and Al in blue. Identical scale for the different maps.

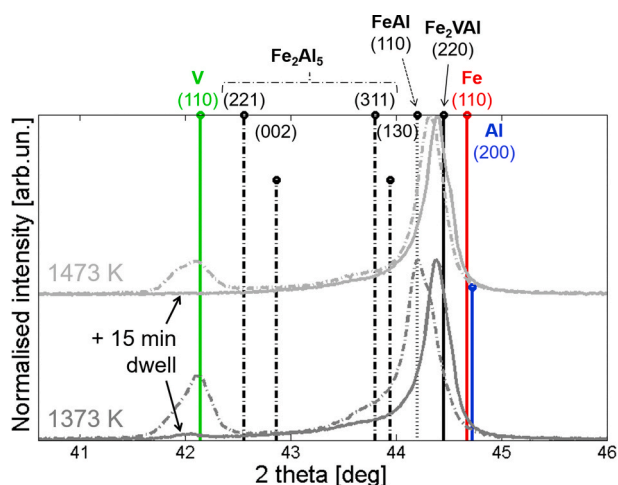


Fig. 5. X-ray diffractograms of mixed elemental powders after heating at 50 K  $\text{min}^{-1}$  up to 1373 K and 1473 K (dashed-dotted lines, similar to Fig. 3) and with an additional dwell of 15 min at the maximal temperature (continuous lines).

phase in order to calculate its relative density. Hence, the resulting pressureless reactively sintered compact only reaches, with an apparent density value of  $3.3 \text{ g cm}^{-3}$ , 50 % of the theoretical density (used previously and stated in Section 2). Fig. 8 also shows that applying the optimum SPS conditions (a 15 min dwell at 1473 K under 40 MPa load) on a mixed elemental powders green pellet, leads to dense sintered compact, with an apparent density of  $6.5 \text{ g cm}^{-3}$  (i.e. around 99 % relative density), i.e. twice the one obtained by pressureless reactive sintering. Correspondingly, the level of open pores drops to 0.1 % (a lower percentage than in samples sintered from pre-alloyed powder, see Section 4.3 and Table 2). As expected and confirmed by the diffractogram of this compact provided in Fig. 9, the  $L2_1$   $\text{Fe}_2\text{VAI}$  phase is formed in these SPS conditions. In addition, the coupling of SEM and EDX analyses shows that Fe, V, and Al are homogeneously distributed and that small rounded pores are present along the prior powder particle boundaries.

## 4. Discussion

### 4.1. Reaction path

The suggested reaction path will be assessed considering the reported analyses for the reactive sintering of Fe-Al. Indeed, the observations reported above showed distinct reactions between Fe and Al first, followed by the reaction with V. Furthermore, no dedicated results were found for the  $\text{Fe}_2\text{VAI}$  compound. Table 1 summarises the EDX and XRD results of pressureless sintering experiments (Section 3.1) while Fig. 10 gives a schematic representation of the reaction path. The Al-rich phase that forms from 873 K to 1173 K was identified as  $\text{Fe}_2\text{Al}_5$ . It is worth noting that the  $\text{Fe}_2\text{Al}_5$  reaction layer does not appear on every Fe particle simultaneously, being the sign of inhomogeneous contacts between the Fe-Al powder particles despite the high pre-compaction load. It is furthermore assumed that the small presence of  $\text{Fe}_2\text{Al}_5$  at room temperature (RT) before any thermal cycle is due to the energetic mixing applied to the elemental powders that could produce some mechanical alloying. However, it is not expected to have any significant influence on the discussed reaction path or on the sintering behaviour owing to its small amount. At higher temperatures (1073–1373 K), the Fe-rich phase corresponding to FeAl grows at the expense of  $\text{Fe}_2\text{Al}_5$  and Fe. It is worth noting that the FeAl phase ( $\alpha_2$ ) is stable over a large Fe-Al composition range. It is thus possible to observe the sole presence of FeAl and V at some stage of the reactive synthesis. According to XRD analyses, the beginning of diffusion of Fe and Al in the V particles occurs from 1173 K. However, the V particles do not react massively with Al, Fe or Fe-Al compounds before 1473 K. From this temperature, EDX profiles show that V progressively diffuses within the FeAl phase. Conversely, it appears that FeAl diffuses significantly in the V particles to form the V-rich ternary phase (first Fe-V-Al row in Table 1), while Al mostly diffuses in V when no FeAl particle is directly in contact with the V in agreement with the binary Al-V phase diagram (second Fe-V-Al row in Table 1). These assumptions are reinforced by the fact that Fig. 3 does not present a diminution of the intensity of the FeAl peak at the expense of the  $\text{Fe}_2\text{VAI}$  one, but rather a progressive displacement of the XRD peak of FeAl towards  $\text{Fe}_2\text{VAI}$  peak position. The composition of the ternary phases does not correspond to any specific phase and is still far from  $\text{Fe}_2\text{VAI}$ . It is worth noting that the composition of the V-enriched FeAl phase at 1473 K in Table 1 is slightly higher than the thermodynamic limit of solubility of V in FeAl at 1023 K, which is around 5–6 at.% [13,14].

Some simulations were performed using the DICTRA-Thermocalc

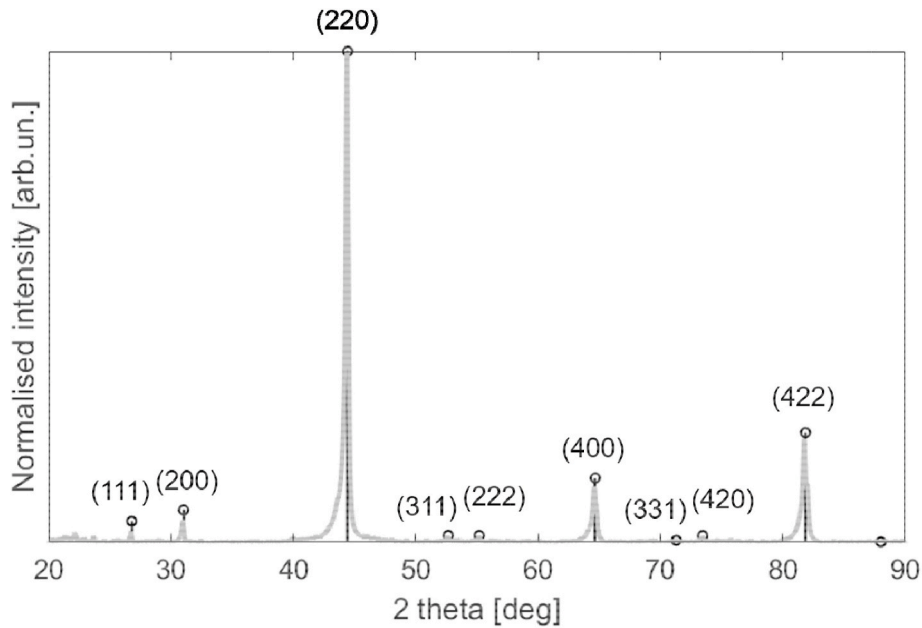


Fig. 6. X-ray diffractogram of mixed elemental powders after heating at  $50 \text{ K min}^{-1}$  up to  $1473 \text{ K}$  with an additional dwell of  $15 \text{ min}$  at the maximum temperature (same full light grey line as Fig. 5). The typical (111) and (200) peaks corresponding to the ordered  $L2_1$   $\text{Fe}_2\text{VAl}$  structure are clearly visible.

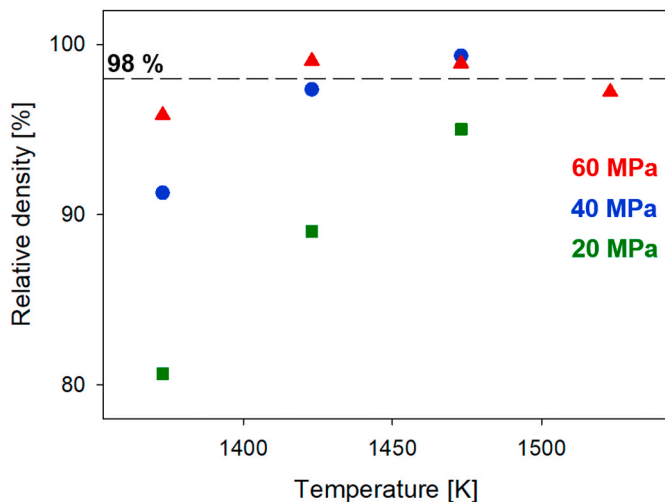


Fig. 7. Evolution of the relative density of sintered samples of pre-alloyed  $\text{Fe}_2\text{VAl}$  powder as a function of the applied pressure and dwell temperature (dwell of  $15 \text{ min}$ ). The horizontal dashed line gives the limit of what is considered as dense samples.

software in order to support the experimental results of Figs. 2 to 5. 1D V-FeAl diffusion couples were simulated with a thickness of the V layer of  $14.4 \mu\text{m}$  (half of the diameter of the largest V particles) and a layer of FeAl of  $30.6 \mu\text{m}$  in thickness (Fig. 11(a)). The initial compositions of both phases at  $1373 \text{ K}$  were taken from Table 1. Fig. 11(b) compares the concentration profiles of the experimental results with the DICTRA simulations. After heating from  $1373 \text{ K}$  to  $1473 \text{ K}$  at  $50 \text{ K min}^{-1}$ , some V diffuses into the FeAl phase but pure V layer remains with a thickness of around  $10 \mu\text{m}$ . At this stage, the mean composition of the FeAl phase is  $64.7 \text{ at.}\% \text{ Fe}$ ,  $7.6 \text{ at.}\% \text{ V}$  and  $27.7 \text{ at.}\% \text{ Al}$ , very similar to the experimental measurements (66-8-26 in Table 1).

Fig. 12 corresponds to the DICTRA simulations with additional dwells at  $1473 \text{ K}$ . After  $15 \text{ min}$ , no more pure V remains, in agreement with Figs. 4 and 5. However, the composition is clearly not yet homogeneous in the whole thickness. Simulation with an additional dwell of

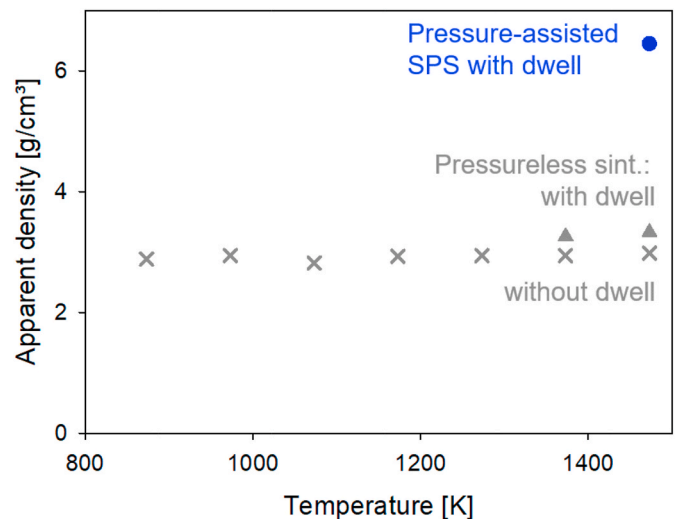
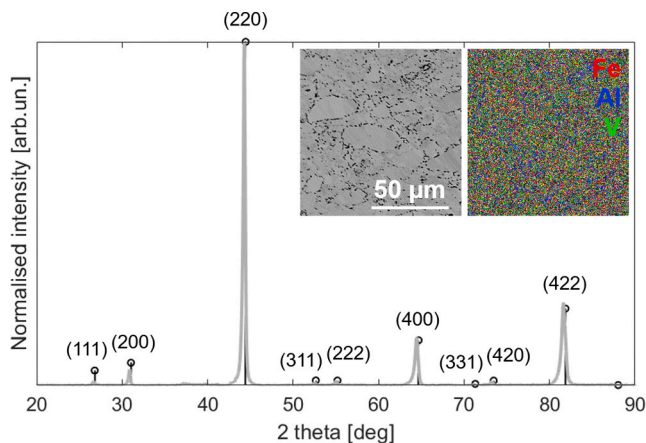


Fig. 8. Comparison of the apparent densities of reactively sintered samples as a function of the maximum temperature.

$45 \text{ min}$  at  $1473 \text{ K}$  leads to a homogeneous composition over distances corresponding to the largest V particles (diam.  $\sim 30 \mu\text{m}$ ).

As demonstrated, due to its higher melting temperature, vanadium diffuses more slowly than Fe and Al and can thus be considered as almost inert in the system up to  $1473 \text{ K}$ . As a consequence, the reaction path below this temperature can be closely related to the reactions occurring in the Fe-Al system. Several authors who considered the synthesis of iron aluminides by pressureless sintering of elemental powders pointed out that various Fe-Al intermetallic compounds form depending on the size of the powder particles, the pre-compacting pressure, the heating rate, and the maximum temperature [5–9]. The present results, summarised in Table 1 and Fig. 10, perfectly fit with the diffusion paths proposed by Gedevisanishvili et al. [6] and Sina et al. [9] in which Al reacts entirely below  $873 \text{ K}$  (for heating rates of  $5$  and  $7.5 \text{ K min}^{-1}$ , respectively). However, both authors agree on the fact that only the FeAl phase remains after heating up to  $1273 \text{ K}$  [6,9], while in the present work some



**Fig. 9.** X-ray diffractogram of mixed elemental powders sintered in the optimum SPS conditions (a 15 min dwell at 1473 K under 40 MPa load) with the theoretical peaks corresponding to the ordered L2<sub>1</sub> Fe<sub>2</sub>VAl structure. Inset, SEM micrograph and corresponding EDX map showing the distribution of Fe, Al, and V.

**Table 1**

Summary of the EDX and XRD analyses during pressureless sintering of pre-compacted mixed elemental powders at 50 K min<sup>-1</sup>. The mean composition of the phases is mentioned (in at. %) when they were clearly identified by EDX. “√” means that the phase is probably present in small quantity (barely identified by XRD but not by SEM/EDX).

Temperature [K]	Identified phases					
	Fe	V	Al	Fe <sub>2</sub> Al <sub>5</sub>	FeAl	Fe-V-Al
RT	>98	>99	>99	✓		
873	>98	>99		34Fe-65Al	✓	
973	>98	>99		34Fe-65Al	✓	
1073	>97	>98		35Fe-64Al	69Fe-30Al	
1173	>95	>99		38Fe-61Al	67Fe-31Al	
1273	82Fe-17Al	>98			58Fe-41Al	
1373		>98			69Fe-29Al	
1473		>97			66Fe-8V-26Al	37Fe-43V-20Al
+15 min						3Fe-78V-19Al 50Fe-27V-23Al 39Fe-40V-21Al

Fe-Al solid solution remains at that temperature (Table 1). It may be explained by the presence of inert V particles that reduce the contacts between Fe and Fe<sub>2</sub>Al<sub>5</sub> particles, thus hindering diffusion.

In the case of the processing of iron aluminides [5–9], DSC or DTA revealed one or two exothermic peaks below the melting temperature of aluminium, depending on the experimental conditions. When two peaks are observed, the onset temperature of the first peak ranges from 800 to 910 K, while the second one is located around 910–930 K [5–7,9]. For the single peak, onset temperatures in the range 845–920 K are reported [7–9]. Fig. 13 shows the DSC curve corresponding to the present mixture of Fe, V, and Al elemental powders. Only one exothermic peak is observed with the onset at 918 K and the maximum at 924 K.

Summarising published results [6–9], one can conclude that a unique exothermic peak is promoted for large heating rates (10 K min<sup>-1</sup> vs 0.5–5 K min<sup>-1</sup>), for fine Fe powder particles (7–10 μm vs 60 μm), and for non-compacted powders. The DSC curve (Fig. 13) is consistent with

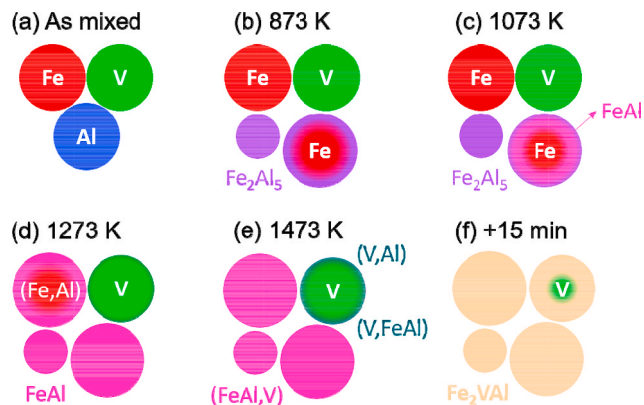


**Fig. 10.** Suggested reaction path during pressureless sintering of pre-compacted mixed elemental powders heated at 50 K min<sup>-1</sup>: (a) initial situation, (b–e) when interrupting the heating cycle at various temperatures, and (f) with an additional dwell of 15 min at 1473 K.

these conclusions since large heating rate (40 K min<sup>-1</sup>) and rather small Fe particles (~22 μm) were used. Furthermore, the powders were only compacted by hand before DSC measurement. However, some discrepancy remains in the interpretation of the origin of the peaks. Gedevisishvili et al. [6] associated the first and second exothermic DSC signals to the formation of Fe<sub>2</sub>Al<sub>5</sub> and to the (partial) formation of FeAl, respectively. On the other hand, Sina et al. [9] claimed that the main exothermic peak corresponds to a combustion reaction leading to the formation of Fe<sub>2</sub>Al<sub>5</sub>, while FeAl is formed by a diffusional reaction between Fe<sub>2</sub>Al<sub>5</sub> and some remaining Fe. The present results seem to agree with this second scenario. Indeed, Table 1 shows that Al is totally consumed during the formation of Fe<sub>2</sub>Al<sub>5</sub> (highly exothermic instantaneous reaction corresponding to the main peak on Fig. 13), whereas Fe<sub>2</sub>Al<sub>5</sub> and FeAl coexist in a larger temperature range, supporting the assumption of a diffusional reaction. It is worth noting that, while no more pure aluminium is identified at 873 K during pressureless sintering (Table 1), the formation of Fe<sub>2</sub>Al<sub>5</sub> occurs at a significantly higher temperature during the DSC measurement (onset at 918 K). This shift may be explained by differences in the preparation of the powders and by the measurement of the temperature (see Fig. 15 and Section 4.2).

The analysis of the DSC peak(s) can give additional information on the enthalpy of the reaction(s). The peak area of Fig. 13 corresponds to an energy of -2.63 J for a sample of 37 mg. It is worth noting that, as shown in Section 3.1, only part of the elemental powders reacts at this temperature. Based on the previous analysis, it can be assumed that the main exothermic DSC peak corresponds to the reaction of the entire Al powder with the appropriate quantity of Fe in order to form Fe<sub>2</sub>Al<sub>5</sub> (9.6 mg according to the total mass). It gives an enthalpy of reaction equals to -252 J g<sup>-1</sup>, significantly smaller than the values found in the literature for the formation of Fe<sub>2</sub>Al<sub>5</sub>: -716 to -866 J g<sup>-1</sup> [15,16]. However, the values of the literature are calculated at 0 K [16] or determined at room temperature [15], while the enthalpies of formation evolve with temperature. Thermocalc simulations were performed and gave -850 J g<sup>-1</sup> at room temperature, in agreement with the -866 J g<sup>-1</sup> value of Gasior et al. [15], and -350 J g<sup>-1</sup> at 920 K. This last value is closer to the -252 J g<sup>-1</sup> of Fe<sub>2</sub>Al<sub>5</sub> found experimentally from the DSC measurements. Another additional explanation could be that the highly exothermic formation of Fe<sub>2</sub>Al<sub>5</sub> could lead to the local melting of Al, which is an endothermic reaction. The main DSC peak of Fig. 13 could thus be the combination of the exothermic peak due to the formation of Fe<sub>2</sub>Al<sub>5</sub> and of the endothermic peak due to the melting of Al. In any case, the presence of one exothermic peak on Fig. 13 confirms the reaction path suggested in the present work and, as considered by Rabin et al. [5], it is the sign that solid-state diffusion at inter-particle contacts may be sufficient to induce the formation of intermetallic compounds.

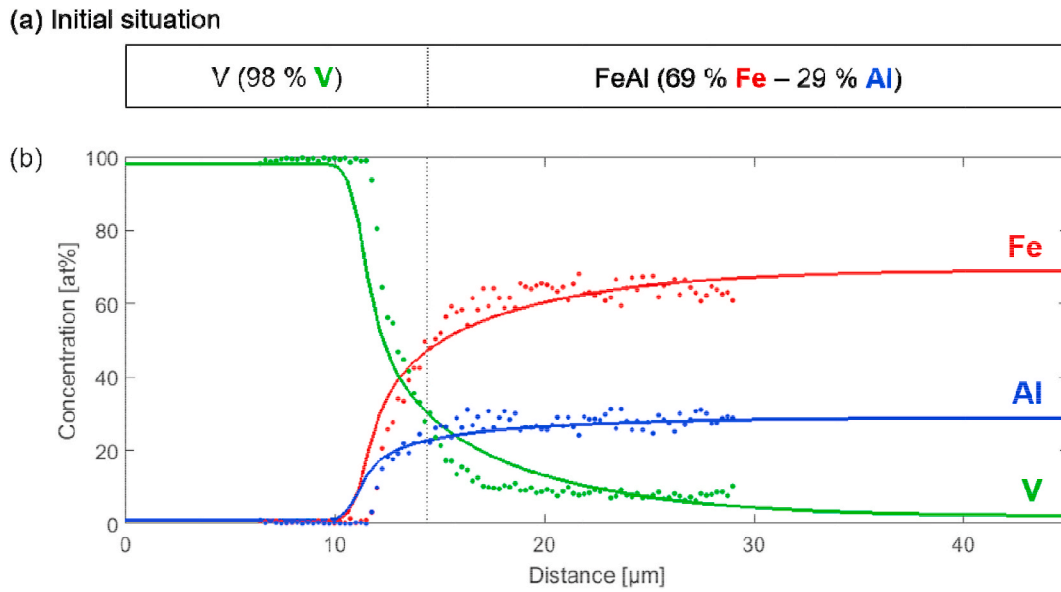


**Fig. 11.** (a) Initial stage of the calculated profiles simulated by DICTRA using as initial conditions the EDX compositions at 1373 K. (b) Experimental (dots) and calculated (lines) concentration profiles at the interface between V and FeAl particles; the experimental profiles are measured after heating mixed elemental powders up to 1473 K at  $50 \text{ K min}^{-1}$ . The vertical dotted line represents the initial position of the interface.

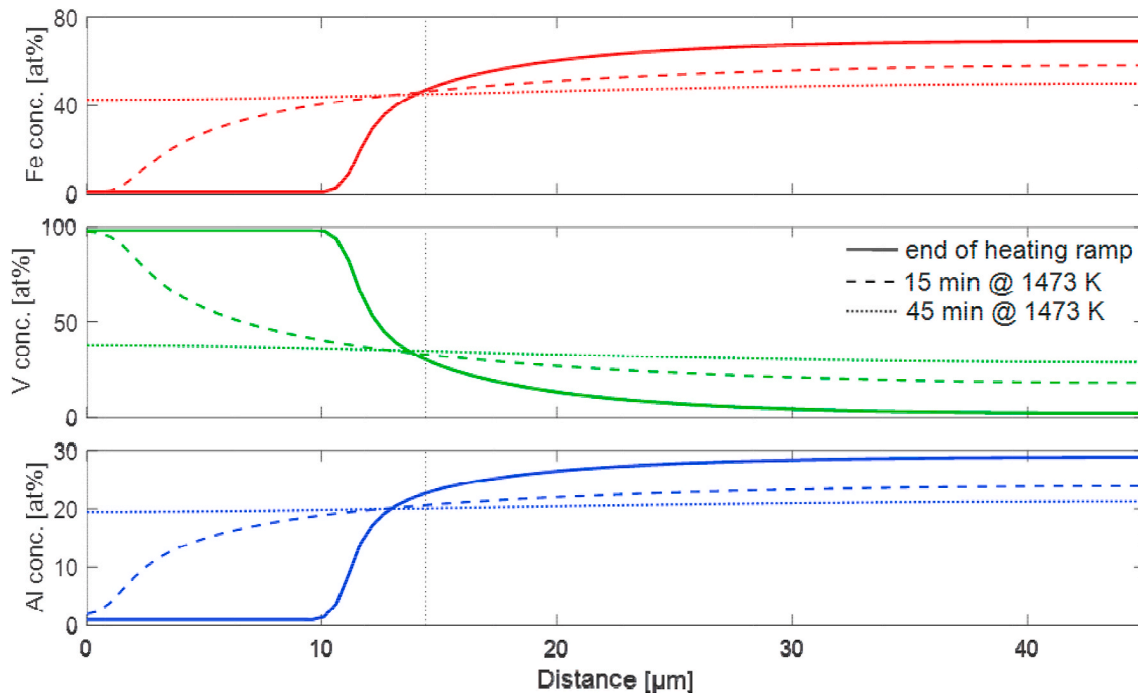


**Fig. 12.** Evolution of the concentration profiles of simulated 1D V-FeAl diffusion couples with the duration of the heat-treatment at 1473 K: at the end of the heating ramp (continuous lines), after 15 min (dashed lines) and after 45 min (dotted lines).

#### 4.2. Densification

Fig. 14 shows the evolution of the relative density of a pre-alloyed powder compact, calculated from the position of the punch after correction for the expansion of the graphite tooling, as a function of time during the heating and dwell steps of a typical SPS cycle. It highlights that the relative density steeply increases near the end of the heating step, in the temperature range 1273–1473 K, hence before the 15 min-dwell. The maximum densification rate is reached at 1404 K. The relative density exceeds the 98 % limit after 2 min of dwell at 1473 K for an applied pressure of 40 MPa while 15 min of dwell brings a slightly higher

final relative density of 99.3 %.

Relative density values higher than 98 % have been obtained after heat treatments of 15 min in the 1423–1473 K temperature range when the applied load is equal or above 40 MPa. This result is in fair agreement with Goto et al. [17] who obtained samples of density around 96–98 % after 1–3 min SPS sintering cycles at 1373 K in vacuum under similar load (40 MPa). The pre-alloyed doped  $\text{Fe}_2\text{VAI}$  powders used by these authors were obtained by crushing arc-melted ingots. The effect of increasing sintering time being usually small compared to the effect of increasing the sintering temperature [18], as confirmed by Fig. 14, the slightly higher temperature needed in the current study to achieve

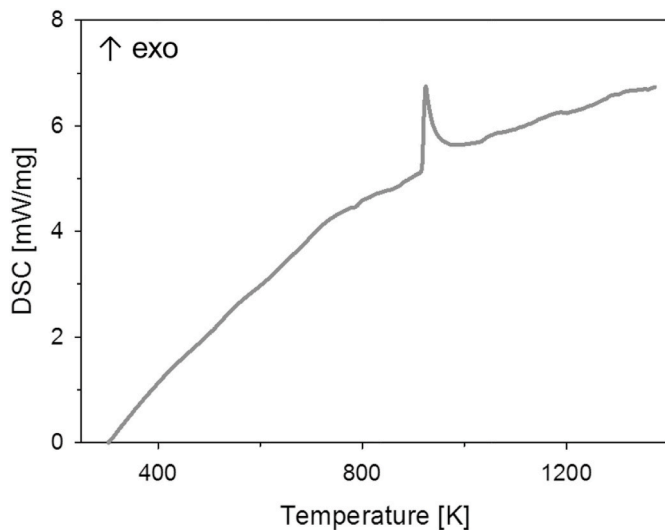


Fig. 13. DSC curve carried out on the mixed elemental Fe, V, and Al powders at a heating rate of  $40 \text{ K min}^{-1}$ . The powders were only manually pressed before DSC measurement.

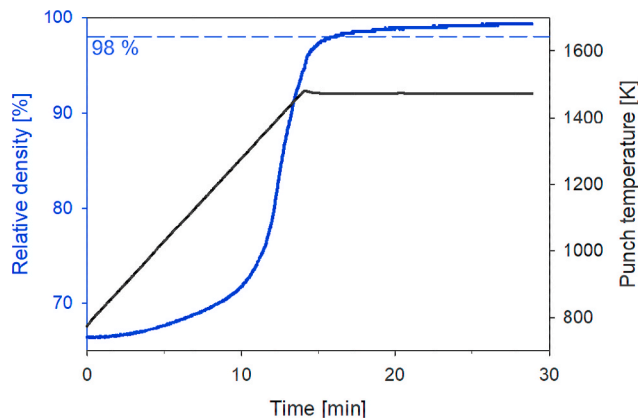


Fig. 14. Evolution of the relative density of a pre-alloyed powder compact (calculated from the punch displacement) and temperature as a function of time during a SPS cycle under an applied pressure of 40 MPa (best sample of Fig. 7). The horizontal dashed line corresponds to the limit of what is considered as dense samples. « Time 0 » has been conveniently set when temperature reached 773 K.

similar density level is probably related to the particle size distribution or initial state of the starting raw material influencing the sintering driving force. Mikami et al. [19,20] also sintered pre-alloyed Si-doped

$\text{Fe}_2\text{VAl}$  powders and reached near-full density samples after 3 min of heat treatment at 1273 K in vacuum under similar level of pressure (40 MPa), hence 200 K below the optimum temperature determined in the current study. Here again, the difference in sintering behaviour is attributed to the nature of the starting powders. Indeed, Mikami et al. used mechanical alloying (i.e. high-energy milling) to synthesize their powders. The resulting fineness of the individual grains with an average size around  $7 \mu\text{m}$  and consisting of sub-micron agglomerated flakes accounts for the higher sinterability of these powders thanks to more pore-solid interface area and promoted volume and grain boundary diffusions. To a lesser extent, the increased quantity of defects generated by mechanical alloying is also beneficial to an increase of the sintering driving force [5,18]. Finally, in the absence of detailed information on the respective SPS configuration used by both Goto et al. [17] and Mikami et al. [19,20], it cannot be ruled out that the difference in sintering temperature also reflects differences in the location where temperature is recorded during the sintering cycle.

Fig. 15 compares the evolution with time of the recorded temperature, relative displacement of the punch (the signature of the height change of the powder compact) and heating power during the heating ramp of the thermal cycle for conventional and reactive SPS. Compared to the curves of the pre-alloyed powder which present a monotonous evolution (Fig. 15(a)), the reactive SPS behaviour of Fe-V-Al powder mixture is characterized by specific features directly related to the reaction path discussed in Section 4.1.

In the initial phase of heating, around 800–810 K, the relative punch displacement abruptly increases, indicating a rapid densification (Fig. 15(b)). The phenomenon is very short, about 20 s, and perfectly coincides with a marked raise of the temperature, well above the imposed nominal temperature set-point, and to a simultaneous decrease of the required heating power, as highlighted by the grey box on Fig. 15 (b). This temperature peak may be associated with the exothermic formation of  $\text{Fe}_2\text{Al}_5$ , as discussed in Section 4.1 and also reported by Paris et al. around 783 K for iron aluminide [10]. Once the formation of Fe-Al intermetallic compounds takes place, the required heating power decreases since the reaction is self-propagating [5,8] and some instantaneous shrinkage occurs, being probably the sign of the transient presence of liquid aluminium. The temperature shift between the formation of  $\text{Fe}_2\text{Al}_5$  in this reactive sintering run (800–810 K) and the one observed during the DSC experiment (onset at 918 K on Fig. 13) may be explained by the difference in pre-compaction pressure used in preparing the powder compacts. Indeed, Sina et al. [9] concluded that combustion occurs at higher temperatures in un-compacted samples due to insufficient contact between the reactant particles, as it is the case for the DSC measurement (only hand compaction was applied, see Section 4.1). On the other hand, the temperature during reactive sintering is not measured as close to the sample as in the DSC equipment. As mentioned in Section 2, the punch temperature is measured 2 mm above the specimen, what may bring some underestimation of the actual specimen

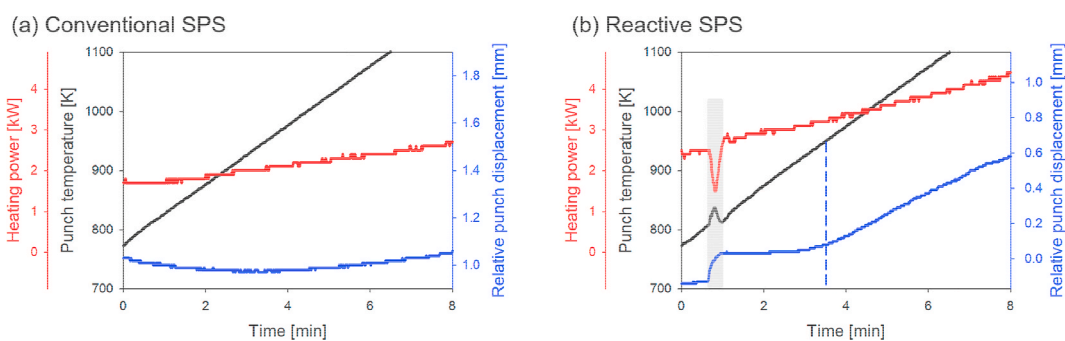


Fig. 15. Evolution with time of the heating power, temperature and relative punch displacement corresponding to the early stages of SPS cycles conducted at a heating rate of  $50 \text{ K min}^{-1}$  (a) in conventional SPS starting from prealloyed powder, and (b) in reactive SPS starting from mixed elemental powders. « Time 0 » has been conveniently set when temperature reached 773 K.

temperature, especially during rapid heating of conductive materials. After the transient behaviour in the 800–820 K temperature range, the relative displacement of the punch starts to increase smoothly around 950 K up to the point when pressure is applied. The 950 K transition, highlighted by the dashed blue line on Fig. 15(b), is expected to correspond to the above-mentioned onset of solid state bonding between particles observed on EDX maps (Section 3.1 and Fig. 2).

#### 4.3. Comparison between the sintered samples

Fig. 16 compares the microstructure of the samples sintered from the pre-alloyed powder and from mixed elemental powders. While samples starting from pre-alloyed powder are relatively clean and present only few vanadium carbide precipitates (Fig. 16(a)), samples manufactured by reactive sintering clearly present more contamination (Fig. 16(b)), the black precipitates corresponding to aluminium oxides. In addition, the reactively sintered sample contains more and smaller rounded pores along the prior powder particle boundaries. Based on the EBSD maps, a mean grain size (i.e. crystallite size) of 38.5  $\mu\text{m}$  and 5.1  $\mu\text{m}$  has been estimated by the mean linear intercept method, respectively. This result should be considered with respect to the initial grain size: 9.7  $\mu\text{m}$  for the pre-alloyed powder (with a mean size of the powder particles of 76  $\mu\text{m}$ ) vs 1.0  $\mu\text{m}$  for the mixed elemental powders (with sizes of the powder particles between 19  $\mu\text{m}$  and 23  $\mu\text{m}$ ), also determined by the mean linear intercept method on EBSD maps of the powders. If the applied sintering conditions lead accordingly to a 4–5 fold increase of the grain size in both cases, it is worth pointing out that starting from the mixed elemental powders mixture enables to achieve an overall finer microstructure.

As confirmed by the XRD measurements (Sections 3.2 and 3.3, especially Fig. 9), (111) and (200) peaks typical of a  $L2_1$  structure are present in both cases, although the sintering temperature of 1473 K is higher than the  $L2_1$  to B2 transition temperature estimated at 1353 K–1390 K in the literature [21,22]. Furthermore, as XRD was performed on bulk samples, it is difficult to characterise precisely the level of ordering as texture may cause some modulations of the relative intensities of the diffraction peaks. Contrarily, Maier et al. [21] and the present authors in a previous work [22] used powder diffraction in order to characterise

order without any disturbance coming from a possible texture. Anyway, the presence of small (111) and (200) peaks shows that both sintered samples present, at least partially, the  $L2_1$  structure what is consistent with the conclusion of Maier et al. that  $\text{Fe}_2\text{VAl}$  crystallizes in the ordered  $L2_1$  structure at room temperature.

Table 2 compares for both types of samples the apparent density and open porosity, together with their Al contents. The sample sintered from mixed elemental powders presents a slightly lower apparent density, which may not be explained by its Al content (it should present a higher density since it contains less Al). While the levels of open porosity are relatively similar, the presence of closed pores and impurities, e.g. alumina (visible on Fig. 16(b)) may be an explanation for the lower apparent density of the reactively sintered sample.

Finally, an important point to conclude the present study is the emphasis on the thermoelectric efficiency of a sample sintered from mixed elemental powders (15 min at 1473 K under 40 MPa). The actual composition of the sample measured by EDX is 49.8 at.% Fe - 27.1 at.% V - 23.1 at.% Al. Fig. 17 presents the temperature dependence of its Seebeck coefficient and its electrical resistivity, together with the resulting power factor. At room temperature, the Seebeck coefficient  $S$  has a value of  $-96 \mu\text{V K}^{-1}$  and the electrical resistivity  $\rho = 7.2 \mu\Omega \text{ m}$ , giving a power factor of  $1.28 \cdot 10^{-3} \text{ W m}^{-1} \text{ K}^{-2}$ . The comparison with the sample sintered from prealloyed powder is however difficult to conduct because the thermoelectric properties are highly dependent on the actual composition of Fe-V-Al compounds [23]. A change of a few tenths of a percent of one element can induce a significant change of the Seebeck coefficient [23]. Anyway, the properties of sintered or arc melted samples with close compositions reported by Goto et al. [17] and Mikami et al. [19,20,23] range for  $S$  from  $-100$  to  $-145 \mu\text{V K}^{-1}$  and for  $\rho$  from 2.5 to 12  $\mu\Omega \text{ m}$  at 350 K. Furthermore, the evolution with temperature of the properties shown on Fig. 17 is also in line with the expected behaviour of  $\text{Fe}_2\text{VAl}$ -based compounds [19,20]. The thermoelectric properties of samples sintered from mixed elemental powders are thus perfectly coherent with samples sintered from pre-alloyed powder or obtained with other melt-grown manufacturing processes, with significant advantages in terms of process (e.g. flexibility, simplicity, rapidity).

## 5. Conclusion

The present work considered reactive sintering as an interesting path to synthesize the thermoelectric  $\text{Fe}_2\text{VAl}$  compound, as it allows easily tuning the composition without any pre-alloying step (either by melting or by mechanical alloying). On the one hand, the reaction path between Fe, V, and Al elemental powders has been studied by EDX and XRD and a comparative assessment has been conducted with the reactive sintering of iron aluminides since V particles stay almost inert in the system up to 1473 K. On the other hand, the conditions of spark plasma sintering to manufacture  $\text{Fe}_2\text{VAl}$ -based compounds for thermoelectric applications have been highlighted. The sintering of coarse pre-alloyed powder via SPS (dwell time of 15 min at 1473 K under 40 MPa) produces sintered parts with relative densities higher than 99 %. In view of the reaction path, these SPS conditions were used for the mixed Fe, V, and Al powders but with pressure applied only from 1273 K. Under these conditions, reactively sintered samples with high relative density were produced. Specific features of the reaction path, e.g. the exothermic formation of  $\text{Fe}_2\text{Al}_5$ , were discussed together with the densification

**Table 2**

Comparison of the apparent density and open porosity of  $\text{Fe}_2\text{VAl}$ -based samples sintered in the same conditions (15 min at 1473 K under 40 MPa) from pre-alloyed powder or from mixed elemental powders.

	Al content [at.% Al]	Apparent density [g.cm <sup>-3</sup> ]	Open porosity [%]
Pre-alloyed	24.3	6.54	0.3
Mixed elemental powders	23.1	6.46	0.1

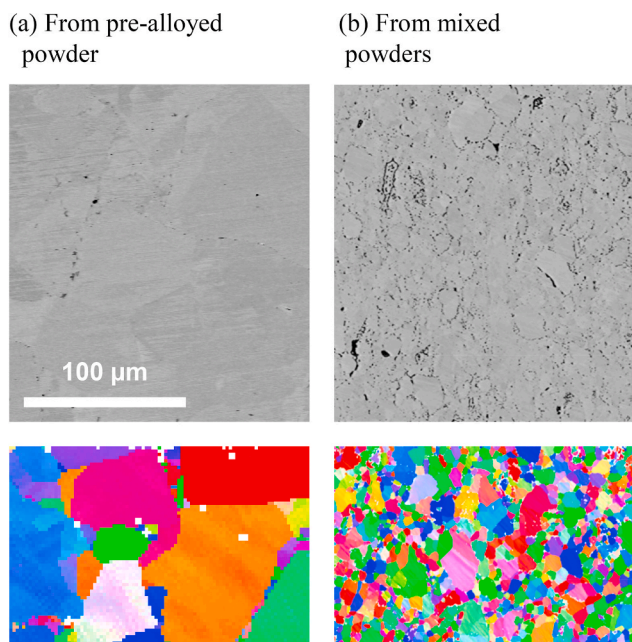


**Fig. 16.** SEM micrographs and EBSD maps of samples sintered for 15 min at 1473 K under 40 MPa starting (a) from pre-alloyed powder or (b) from mixed elemental powders. Identical scale for the different images.

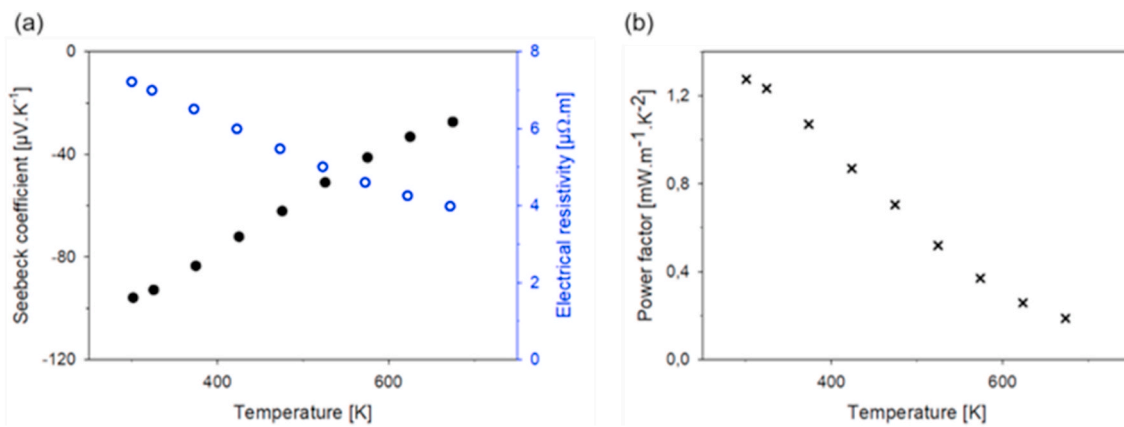


**Fig. 17.** Temperature dependence of Seebeck coefficient and electrical resistivity (a), and calculated power factor (b), of a sample sintered from mixed elemental powders in optimized SPS conditions (15 min at 1473 K under 40 MPa).

behaviour of the mixed elemental powders. Finally, the Seebeck coefficient of such samples is similar to samples sintered from pre-alloyed powder or grown from the melt, which is a unique result in the thermoelectric community. In view of the first promising thermoelectric properties of reactively sintered sample, a systematic assessment of optimized compositions around the stoichiometric  $\text{Fe}_2\text{VAl}$  compound will be conducted to further develop this original processing route.

#### CRediT authorship contribution statement

**Camille van der Rest:** Conceptualization, Investigation, Validation, Visualization, Writing - original draft. **Vedi Dupont:** Resources, Investigation. **Jean-Pierre Erauw:** Conceptualization, Writing - review & editing. **Pascal J. Jacques:** Conceptualization, Writing - review & editing, Supervision.

#### Declaration of competing interest

The authors declare that they have no known competing financial interests or personal relationships that could have appeared to influence the work reported in this paper.

#### Acknowledgments

The authors acknowledge the financial support from the European Funds for Regional Developments (FEDER) and the Walloon Region in the framework of the operational program “Wallonie-2020.EU” (project: Multifunctional thin films/LoCoTED). The authors are grateful to ULB for the DSC measurements.

#### References

- [1] H.J. Goldsmid, *Introduction to Thermoelectricity*, first ed., Springer-Verlag Berlin Heidelberg, 2009.
- [2] B.A. Cook, J.L. Harringa, Solid-state synthesis of thermoelectric materials, in: D. M. Rowe (Ed.), *Thermoelectrics Handbook - Macro to Nano*, CRC Press, Taylor & Francis Group, 2006 chap. 19.
- [3] W. Schatt, K.-P. Wieters (Eds.), *Powder Metallurgy: Processing and Materials*, European Powder Metallurgy Association, 1997.
- [4] Y.M. Belov, S.M. Maniakin, I.V. Morgunov, Review of methods of thermoelectric materials mass production, in: D.M. Rowe (Ed.), *Thermoelectrics Handbook - Macro to Nano*, CRC Press, Taylor & Francis Group, 2006 chap. 20.
- [5] B.H. Rabin, R.N. Wright, Synthesis of iron aluminides from elemental powders: reaction mechanisms and densification behaviour, *Metall. Trans. A* 22 (1991) 277–286.
- [6] S. Gedevanishvili, S.C. Deevi, Processing of iron aluminides by pressureless sintering through Fe + Al elemental route, *Mater. Sci. Eng. A* 325 (2002) 163–176.
- [7] S. Jozwiak, K. Karczewski, Z. Bojar, Kinetics of reaction in FeAl synthesis studied by the DTA technique and JMA model, *Intermetallics* 18 (2010) 1332–1337.
- [8] P. Novak, A. Michalcova, I. Marek, M. Mudrova, K. Saksl, J. Bednarcik, P. Zikmund, D. Vojtech, On the formation of intermetallics in Fe-Al system - an in situ XRD study, *Intermetallics* 32 (2013) 127–136.
- [9] H. Sina, J. Corneliusson, K. Turba, S. Iyengar, A study on the formation of iron aluminide (FeAl) from elemental powders, *J. Alloys Compd.* 636 (2015) 261–269.
- [10] S. Paris, E. Gaffet, F. Bernard, Control of FeAl composition produced by SPS reactive sintering from mechanically activated powder mixture, *J. Nanomater.* 2013 (2013). Article ID 150297.
- [11] O. Guillon, J. Gonzalez-Julian, B. Dargatz, T. Kessel, G. Schiering, J. Rathel, M. Herrman, Field-assisted sintering technology/Spark plasma sintering: mechanisms, materials, and technology developments, *Adv. Eng. Mater.* 16 (2014) 830–849.
- [12] C.S. Morgan, K.H. McCorkle, G.L. Powell, Sintering and desintering of thoria, *Mater. Sci. Res.* 6 (1973) 293–299.
- [13] T. Maebashi, T. Kozakai, M. Doi, Phase equilibria in iron-rich Fe–Al–V ternary alloy system, *Z. Metallkd.* 95 (2004) 11.
- [14] V. Raghavan, Al-Fe-V (Aluminum-Iron-Vanadium), *J. Phase Equilibria Diffus.* 27 (2006) 3.
- [15] W. Gasior, A. Debski, Z. Moser, Formation enthalpy of intermetallic phases from Al-Fe system measured with solution calorimetric method, *Intermetallics* 24 (2012) 99–105.
- [16] G. Wu, Y. Ren, J. Zhang, K. Chou, Contribution of Ti addition to the electronic structure and adhesion at the  $\text{Fe}_2\text{Al}_5/\text{Fe}$  interface in 55%Al-Zn coating, *TMS suppl., SAVE Proc.* 1 (2012).
- [17] H. Goto, Y. Terazawa, M. Mikami, T. Takeuchi, The effect of element substitution on electronic structure, electron transport properties, and lattice thermal conductivity of  $\text{Fe}_2\text{VAl}$  thermoelectric material, *Mater. Trans.* 51 (2010) 2139–2144.
- [18] J.S. Hirschhorn, *Introduction to Powder Metallurgy*, American Powder Metallurgy Institute, 1969.
- [19] M. Mikami, A. Matsumoto, K. Kobayashi, Synthesis and thermoelectric properties of microstructural Heusler  $\text{Fe}_2\text{VAl}$  alloy, *J. Alloys Compd.* 461 (2008) 423–426.
- [20] M. Mikami, K. Kobayashi, T. Kawada, K. Kubo, N. Uchiyama, Development of high-strength  $\text{Fe}_2\text{VAl}$  thermoelectric module designed for a motorcycle, *Int. Conf. Thermoelectrics* (2007) 314–317.
- [21] S. Maier, S. Denis, S. Adam, J.-C. Crivello, J.-M. Joubert, E. Alleno, Order-disorder transitions in the  $\text{Fe}_2\text{VAl}$  Heusler alloy, *Acta Mater.* 121 (2016) 126–136.
- [22] C. van der Rest, A. Schmitz, P.J. Jacques, On the characterisation of antisite defects and ordering in off-stoichiometric  $\text{Fe}_2\text{VAl}$ -based Heusler compounds by X-ray anomalous diffraction, *Acta Mater.* 142 (2018) 193–200.
- [23] M. Mikami, M. Inukai, H. Miyazaki, Y. Nishino, Effect of off-stoichiometry on the thermoelectric properties of Heusler-type  $\text{Fe}_2\text{VAl}$  sintered alloys, *J. Electron. Mater.* 45 (2016) 1284–1289.